Article

An Operational Downscaling Method of Solar-Induced Chlorophyll Fluorescence (SIF) for Regional Drought Monitoring

Zhiming Hong [1] , Yijie Hu [2], Changlu Cui [1], Xining Yang [3], Chongxin Tao [1,4] , Weiran Luo [5], Wen Zhang [1], Linyi Li [1] and Lingkui Meng [1,*]

1   School of Remote Sensing and Information Engineering, Wuhan University, Wuhan 430079, China;
    simonhong@whu.edu.cn (Z.H.); 2016282130106@whu.edu.cn (C.C.); taochx@whu.edu.cn (C.T.);
    wen_zhang@whu.edu.cn (W.Z.); lilinyi@whu.edu.cn (L.L.)
2   National Disaster Reduction Center of China, Beijing 100124, China; huyijie@ndrcc.org.cn
3   Department of Geography and Geology, Eastern Michigan University, Ypsilanti, MI 48197, USA;
    xining.yang@emich.edu
4   School of Management, Xinjiang Agricultural University, Urumqi 830052, China
5   School of Water Conservancy Sciences and Engineering, Zhengzhou University, Zhengzhou 450001, China;
    luowr2012@163.com
*   Correspondence: lkmeng@whu.edu.cn

Abstract: Solar-induced chlorophyll fluorescence (SIF) has been shown to be a powerful proxy for photosynthesis and a promising indicator of drought monitoring, but the ability of high-resolution satellite-derived *SIF* for drought monitoring has not been widely investigated due to a lack of data. The lack of high spatiotemporal resolution satellite *SIF* hinders the resolution enhancement of *SIF* derived by downscaling or reconstruction algorithms. The TROPOspheric Monitoring Instrument (TROPOMI) *SIF* provides an alternative with finer spatiotemporal resolution. We present an operational downscaling method to generate 500 m 16-day *SIF* (TSIF) using Neural Networks over a local spatiotemporal window. The results showed that our method is very robust against overfitting, and TSIF has a strong spatiotemporal consistency with TROPOMI *SIF* (TROPOSIF) with $R^2 = 0.956$ and RMSE = $0.054 \text{ mWm}^{-2}\text{sr}^{-1}\text{nm}^{-1}$. Comparison with another *SIF* product (CASIF) showed a spatiotemporal consistency with TSIF. Comparison with tower gross primary productivity (GPP) from AmeriFlux in California showed a strong correlation with R^2 for multiple ecosystems ranging from 0.58 to 0.88. We explored the capacity of TSIF for monitoring a drought event in Henan, China, showing that TSIF is more sensitive to drought and precipitation compared to the Enhanced Vegetation Index. Our TSIF is a very promising indicator for regional drought monitoring.

Keywords: drought monitoring; SIF; downscaling; TROPOMI

1. Introduction

Solar-induced chlorophyll fluorescence (SIF) has been shown to be a powerful proxy for photosynthesis and gross primary productivity (GPP) [1]. Unlike conventional vegetation indices (e.g., Normalized Difference Vegetation Index NDVI and Enhanced vegetation index EVI) that only look at vegetation "greenness" or are just indicators of vegetation photosynthetic capacity [2], *SIF* probes into a plant's photosynthetic machinery and has the ability to capture vegetation's actual photosynthetic activity and its response to rapid changes in environmental conditions such as light levels and water stress [3–5], making it a crucial tool for vegetation drought monitoring. The advent of satellite *SIF* retrieval is an exciting breakthrough in the ability to monitor global plant photosynthetic activity. Since the first satellite-derived *SIF* from the Japanese Greenhouse Gases Observing Satellite (GOSAT) was produced by Frankenberg [6] and Joiner et al. [7], several other satellite *SIF* measurements have been retrieved using different algorithms or observations, such as from Global Ozone Monitoring Experiment-2 (GOME-2), Scanning Imaging Absorption Spectrometer for Atmospheric Chartography (SCIAMACHY), Orbiting Carbon Observatory-2

(OCO-2) [8], Chinese Carbon Dioxide Observation Satellite Mission (TanSat) [9], and TRO-POspheric Monitoring Instrument (TROPOMI) [10]. In the case of *SIF* retrievals from GOSAT, GOME-2 SCIAMACHY, their coarse spatiotemporal resolutions (10.5 km circle, 40 km × 40 km, and 30 km × 60 km, respectively) seriously hinders applications for fine-scale drought monitoring. OCO-2 and TanSat have high spatial resolution *SIF* products at 1.3 km × 2.25 km and 1 km × 2 km, respectively, but their sparse sampling strategy and long revisit cycles seriously reduce their usability as they have to be aggregated to coarse spatiotemporal resolutions (e.g., monthly and 1° × 1°) for applications. To enhance the spatial resolution of satellite *SIF* or reconstruct high-resolution and spatially continuous *SIF* products, significant effort has been put into the generation of downscaled or reconstructed *SIF* using other satellite data, such as SIF_{LUE} derived from GOME-2 *SIF* by Duveiller [11], GOSIF from OCO-2 *SIF* by Li [12], CSIF from OCO-2 by Zhang [13], $\overline{SIF}_{oco2\_005}$ from OCO-2 by Yu [14], $\overline{SIF}_{005}$ from SCIAMACHY, and GOME-2 by Wen [15]. However, most of these *SIF* datasets have a coarse resolution of 0.05° which is not sufficient for drought monitoring in smaller regions and at a fine scale, especially for agricultural applications. The main challenge to further resolution improvements of *SIF* products is the lack of finer spatiotemporal satellite SIF. Moreover, existing downscaled *SIF* or reconstructed *SIF* have one or more issues that limit their applications. First, *SIF* datasets are not updated frequently, making it difficult to obtain new SIF. Second, for some *SIF* products (e.g., GOSIF), global samples are needed to train a universal global model, which is a model that uses all data for training without time and space stratification [1]. Third, the *SIF* derived from very coarse satellites, such as GOME-2, is not suitable for generating very high-resolution downscaled SIF. Fourth, for local models, such as $\overline{SIF}_{oco2\_005}$, it is impossible to train local models in small regions due to the sparse sampling strategy and long revisit cycle. Fortunately, TROPOMI provides an alternative *SIF* data source (TROPOSIF) which has a spatially contiguous *SIF* with a 16-day revisit and 7 km × 3.5 km resolution at nadir (5.5 km × 3.5 km since 2019) and nearly daily global coverage, making it an ideal data source for *SIF* downscaling at a small regional scale and high spatial resolution. The idea of using time or space constraints to train a local model has been widely applied in LST downscaling studies [16,17]. Some researchers have also introduced such an idea for *SIF* downscaling [11,14,15]. For example, Yu [14] built local models by stratifying biomes and times for training and predictions and showed that local models performed better than a universal model, but further discussion was not performed.

The use of *SIF* for drought monitoring has been widely explored [18–21]. There is wide evidence that *SIF* at coarse resolution (e.g., 0.05°) is a promising drought indicator. However, using *SIF* at finer spatial resolution (e.g., 500 m) for drought monitoring has not been widely explored because of the lack of high-resolution *SIF* products.

In this paper, we presented an operational downscaling method of TROPOSIF. We used TROPOSIF data and the Moderate Resolution Imaging Spectroradiometer (MODIS) data in the same area and date for training and prediction of local models. We then examined our local models' performance by comparing our downscaled TSIF with TROPOSIF. Moreover, we tested our local models' robustness against overfitting. To further validate our downscaled TSIF, we made a comparison with CASIF and Tower GPP in California. Finally, we applied our TSIF to monitor the Henan drought event in July 2019. Our results show that our method will benefit regional drought monitoring at a fine scale.

2. Materials and Methods

2.1. Study Area

Our study area is Henan Province, located in central China. Henan is one of the most important grain-producing areas of China and has suffered frequent droughts in recent years. Henan has a temperate climate that is humid subtropical to the south of the Yellow River and bordering on humid continental to the north. It has a distinct seasonal climate with a windy and dry spring, a hot and humid summer, a sunny and cool autumn, and a cold and dry winter. Summer receives the majority of the annual precipitation, which

decreases from the southeastern to the northwestern portions of the province. The mainland cover types of Henan are cropland, deciduous broadleaf forests, and savannas (Figure 1).
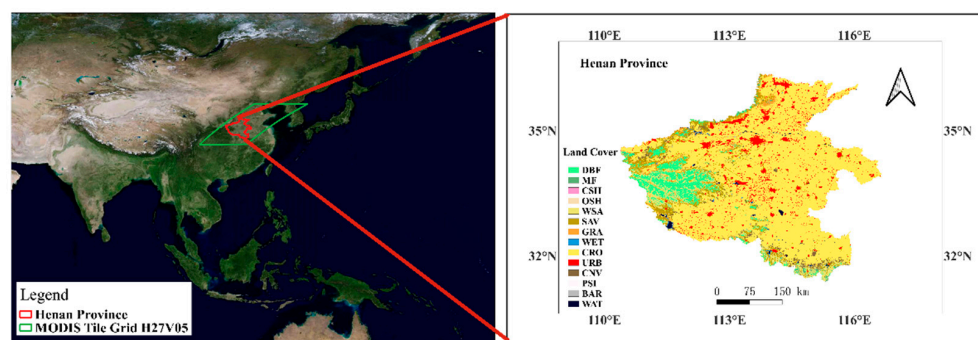

Figure 1. The land cover types of Henan Province. Here, the land cover types are from the MCD12Q1.006 land cover dataset (International Geosphere-Biosphere Programme (IGBP) classification scheme) for the year 2019. The abbreviations are as follows: DBF, Deciduous Broadleaf Forests; MF, Mixed Forests; CSH, Closed Shrublands; OSH, Open Shrublands; WSA, Woody Savannas; SAV, Savannas; GRA, Grasslands; WET, Permanent Wetlands; CRO, Croplands; URB, Urban and Built-up Lands; CNV, Cropland/Natural Vegetation Mosaics; PSI, Permanent Snow and Ice; BAR, Barren; WAT, Water Bodies.

2.2. Data

2.2.1. MODIS Data

In this paper, BRDF-corrected surface reflectance data bands (Band1, Band2, Band3, Band4, Band5, and Band7) from MCD43A4.061, Leaf Area Index (LAI), and fPAR from MCD15A2H.061 were used as the explanatory variables of our downscaling models. We did not use the band Band6 of MCD43A4 because it had too many missing data in our study area and the performance of the downscaling models with or without Band6 did not change much. We did not select too many explanatory variables (e.g., evapotranspiration ET and land surface temperature LST), because too many variables may increase uncertainty and reduce the usability of satellite data caused by data gaps. Of the explanatory variables, reflectance data has been widely used in previous work on *SIF* downscaling [13–15]; fPAR is the import component of *SIF* [22], and LAI is related to the escape factor of the *SIF* yield. Prior to model training, MODIS data were temporally aggregated to 16-day for prediction and then spatially aggregated to 10 km 16-day for training and validating downscaling models. The spatial resolution of the aggregated MODIS data corresponds to 20 × 20 pixels of original MODIS data in the Sinusoidal coordinate reference system. During the aggregation process, pixels of MCD43A4 data with Mandatory_Quality = 255 were discarded, for MCD15A2H, pixels with SCF_QC = 100 were discarded. The coarser aggregated pixels containing fewer than 200 pixels from the original MCD43A4 or MCD15A2H were also discarded. Moreover, the MCD12Q1.006 land cover dataset was aggregated by assigning the vegetation type with the highest area percentage. All the aggregated pixels labeled as urban and built-up lands, permanent snow and ice, barren, and water bodies were also excluded.

2.2.2. TROPOSIF from TROPOMI

We used TROPOSIF from the TROPOMI spectrometer onboard the Sentinel-5 Precursor satellite as our *SIF* data source [23]. The Sentinel-5 Precursor has a wide swath of 2600 km and a 16-day orbital period with an overpass time of 13:3 with the ability to provide nearly daily global coverage. Only TROPOSIF L2B data are available at https://s5p-troposif.noveltis.fr (accessed on 20 December 2021) from May 2018 to November 2021. The TROPOSIF instantaneous estimates are derived from a data-driven approach based on a linear forward model fitting Top of Atmosphere (TOA) radiance in the far-red spectral region including SIF_735 from window 743–758 nm and SIF_735 from window

735–758 nm [10]; the daily average SIF_Corr_735 and SIF_Corr_743 were also created using Frankenberg's method [6] to account for variations in overpass time, length of day, and solar zenith angle. Compared to the earlier *SIF* observation satellite instruments, TROPOMI has relatively high spatial and temporal resolution and a dense sampling strategy. Because SIF_Corr_743 (SIF_743) is more robust to atmospheric effects compared to SIF_Corr_735 (SIF_735) [10], we selected SIF_Corr_743 as our model output variable. TROPOSIF data were spatially and temporally aggregated to 10 km 16-day grid cells to match the aggregated MODIS data. To control *SIF* data quality and reduce uncertainties, the grid cells with less than five TROPOSIF soundings and the grid cells labeled as urban and built-up lands, permanent snow and ice, barren, and water bodies were also excluded. For a detailed description of TROPOSIF data, please refer to https://s5p-troposif.noveltis.fr (accessed on 20 December 2021).

2.2.3. GPP and *SIF* in California

The *SIF* dataset (CASIF) for California used here refers to the daily *SIF* at 500-m resolution developed by Turner et al. [24,25] using an oversampling and downscaling algorithm. CASIF was used as a comparison for our TSIF. In addition, we used the tower GPP estimates from AmeriFlux eddy covariance sites in California to validate the SIF-GPP relationship between TSIF and tower GPP. Here we used six eddy covariance sites following Tuner et al. [24] (Table 1).

Table 1. AmeriFlux eddy covariance sites used in this paper [24].

Site ID	Site Name	Longitude	Latitude	Vegetation Type
US-Bi2	Bouldin Island Corn	121.5350	38.1090	cropland
US-Ton	Tonzi Ranch	120.9660	38.4316	woody savannas
US-Var	Vaira Ranch	120.9507	38.4133	grasslands
US-Tw1	Twitchell Island West Pond	121.6469	38.1074	permanent wetlands
US-Tw4	Twitchell Island East End	121.6414	38.1030	permanent wetlands
US-Tw5	Twitchell Island East Pond	121.6426	38.1072	permanent wetlands

2.2.4. Other Data

To characterize the drought event in our study area, we also used the monthly Standardized Precipitation-Evapotranspiration Index (SPEI) data with a resolution of $1°$ (https://spei.csic.es/map/maps.html/ (accessed on 20 December 2021)) and monthly precipitation from Climate Hazards Group InfraRed Precipitation with Station Version 2.0 (Chirps2) with a resolution of $0.05°$ (https://data.chc.ucsb.edu/products/CHIRPS-2.0/ (accessed on 20 December 2021)). The anomalies of monthly precipitation were calculated using Chirps2 monthly precipitation from 1981 to 2021.

2.3. Model Development and Validation

In this paper, we used Neural Networks (NN) to downscale TROPOSIF. NN is a classical machine learning method that has been successfully used for downscaling SIF, land surface temperature, and soil moisture [13,14,16,26]. NN are a series of computational nodes (called neurons) structured in a single or multi-layer architecture. Every node is connected with all nodes in the previous layer and the next layer. The node values are derived using the activation function (e.g., ReLu) with a pre-activated value, i.e., the weighted sum of all nodes in the previous layer and biases. The NN downscaling model is trained to minimize the loss function to get the best weights and biases [2]. We built local downscaling models for each 10 km 16-day aggregated TROPOSIF using the aggregated MODIS data within the MODIS tile grid of H27V05 which covers the entire Henan Province. The 500 m 16-day aggregated MODIS data were used for *SIF* prediction. We used the data within the MODIS tile grid of H27V05 rather than only within our study area to ensure an adequate sample size. For each local downscaling model, the training data were normalized by their mean and standard deviation. The validation data and prediction data were also normalized by the same mean and standard deviation. Because our method uses

the data in the same area and time for training and prediction, and the training data and validation data are from the aggregation of data used for prediction, such data have similar features which can reduce the errors introduced by data with different spatiotemporal features and distribution. We used the classic machine learning framework Tensorflow (https://tensorflow.google.cn/ (accessed on 25 December 2021)) and set the NN models as a 4-layer network with each hidden layer containing 16 neurons, RMSE as the loss function, Adam as the gradient descent function, learning rate as 0.001, and 40 epochs. In order to prevent overfitting, we also set mindelta = 0.002 and patience = 5 as the early stopping conditions. We first trained a universal model using all TROPOSIF and MODIS data; then, we used it as a pre-trained model to initialize our local models. To train a local model, only TROPOSIF and MODIS data of specific dates were used to generate samples; for example, to train the local model on 12 July 2019, we used the aggregated TROPOSIF and MODIS data on 12 July 2019 (here the date is the first day of 16-day aggregation). We then divided samples into a training dataset (70%) and a validation dataset (30%). Finally, we built the local downscaled models based on these training datasets and validation datasets.

We verified the performance of our downscaling models by calculating R^2 and RMSE for training and validation and the probability distribution of our *SIF* estimation errors following Li et al. [12]. We also calculated the mean and the 5th and 95th percentile of *SIF* of all pixels from TROPOSIF and TSIF. We also made a pixel-by-pixel comparison of TSIF with TROPOSIF to validate their temporal correlation. In addition, we tested the robustness of our method against overfitting by setting the numbers of the hidden layers from 1, 2, 3, 4, and the numbers of neurons of the hidden layers 8, 16, 32, 64. We also made a comparison in the spatial and temporal patterns between TROPOSIF and TSIF. Moreover, for further validation, we compared TSIF with CASIF tower GPP from AmeriFlux eddy covariance sites in California. During the validation process, we also took the universal model as a comparison; the *SIF* generated by the universal model is called USIF.

2.4. Drought Monitoring Analysis of SIF

To validate the drought monitoring performances of our downscaled TSIF, we applied it to monitor the Henan drought event of July 2019. We explored the response of *SIF* and EVI to the drought. We also used SPEI, the anomalies of precipitation, to characterize the spatial and temporal patterns of the drought. Due to the short period of TROPOMI, the anomalies of TSIF could not be calculated. We set 2018 as the reference year and calculated the relative difference defined in Equation (1) to monitor the drought event. The method is similar to that of Yu et al. [14] who used the difference in *SIF* between two years for drought monitoring. Our method shows the relative changes in *SIF* between two years that may be caused by drought, which makes every pixel comparable.

$$\text{Variable} - \text{Diff} = (\text{Variable}_{2019} - \text{Variable}_{2018}) / \text{Variable}_{2018} \times 100 \tag{1}$$

where Variable-Diff could be TSIF-Diff for TSIF, TROPOSIF-Diff for TROPOSIF, USIF-Diff for USIF, or EVI-Diff for EVI. Variable_{2018} indicates that the variable is for 2018, while Variable_{2019} is for 2019. Negative Variable-Diff means the occurrence of drought and positive Variable-Diff means no drought occurs. Of course, the drought is just relative to the reference year.

3. Results

3.1. Model Development and Validation

3.1.1. Performance Validation of the Models

We built 82 local downscaling models for 82 10 km 16-day aggregated TROPOSIF data corresponding to 82 dates. Figure 2 shows the determination coefficient R^2, RMSE of TROPOSIF and TSIF for training and validation and TROPOSIF mean within the MODIS tile H27V05. For training, there were 34 models with $R^2 > 0.85$, 34 models with $R^2 > 0.75$, and 10 models with $R^2 > 0.65$. For validation, there were 32 models with $R^2 > 0.85$, 29 models

with $R^2 > 0.75$, and 19 models with $R^2 > 0.65$. Most RMSE were below 0.07 for both training and validation. In general, the R^2 and RMSE for validation were very close to those for training indicating no overfitting occurred. Interestingly, the RMSE has a strong seasonality similar to those of TROPOSIF. RMSE peak in July or August and reach a valley in November or December. One possible reason is that sufficient precipitation in the growing season reduces our models' prediction performance, but in general, our models perform well.
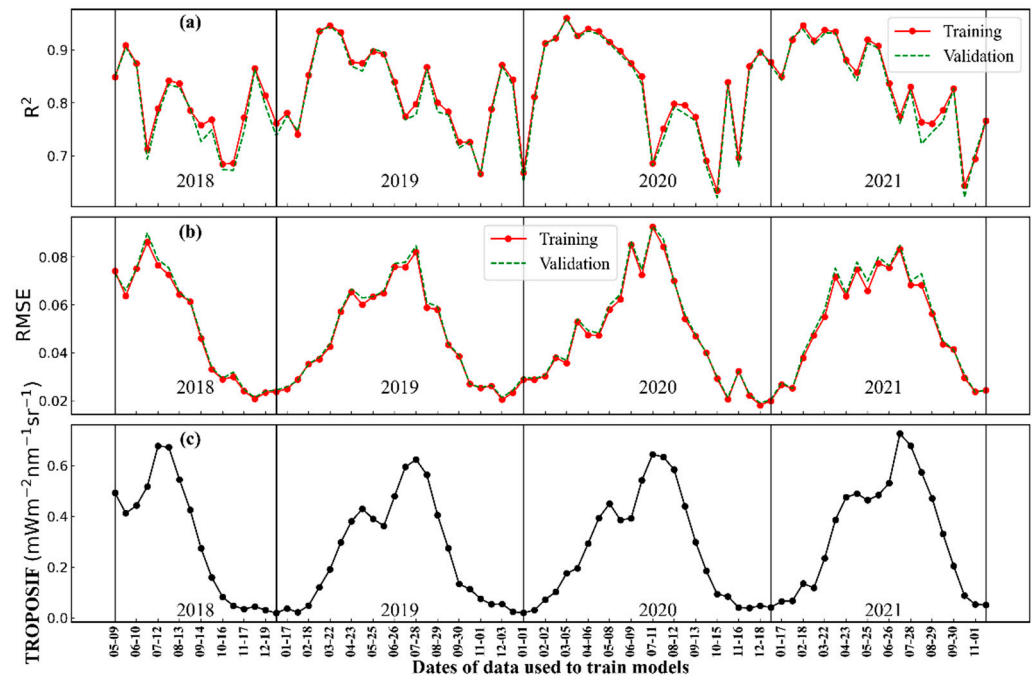
Figure 2. (**a**) The determination coefficient R^2 and (**b**) RMSE of TROPOSIF and predicted TSIF for training and validation; (**c**) The TROPOSIF mean of all *SIF* pixels within MODIS tile grid H27V05.

We calculated the probability distribution of *SIF* prediction residuals (Figure 3). We found that the residuals between our TSIF and TROPOSIF were within ± 0.05 mWm^{-2}sr^{-1}nm^{-1} for the majority of the pixels and the distribution was approximate to the normal distribution. The results suggest that our models predict *SIF* well.

To further estimate the overall accuracy of our method, we then pooled all training data and all validation data, respectively, and drew the scatterplots of TROPOSIF and predicted SIF. As shown in Figure 4, we had a good prediction accuracy with the determination coefficients $R^2 = 0.958$ and RMSE = 0.053 for training and $R^2 = 0.956$ and RMSE = 0.054 for validation. For the universal model, $R^2 = 0.937$ and RMSE = 0.065 were used for both training and validation. Moreover, we also re-aggregated the predicted *SIF* to 10 km and drew the scatterplots of TROPOSIF and the re-aggregated SIF. As shown in Figure 5, we also had a good prediction accuracy with $R^2 = 0.951$ and RMSE = 0.058 for our local models and $R^2 = 0.933$ and RMSE = 0.067 for the universal model. This means that our local models only performed slightly better than the universal model. A similar comparison made by Yu [14] also showed a similar R^2 for the universal and the local models.
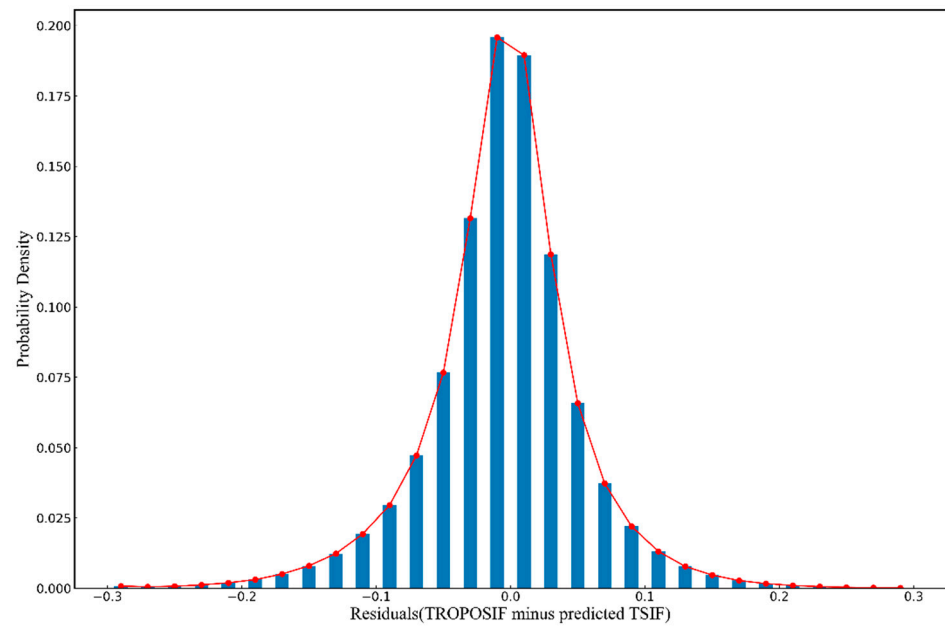
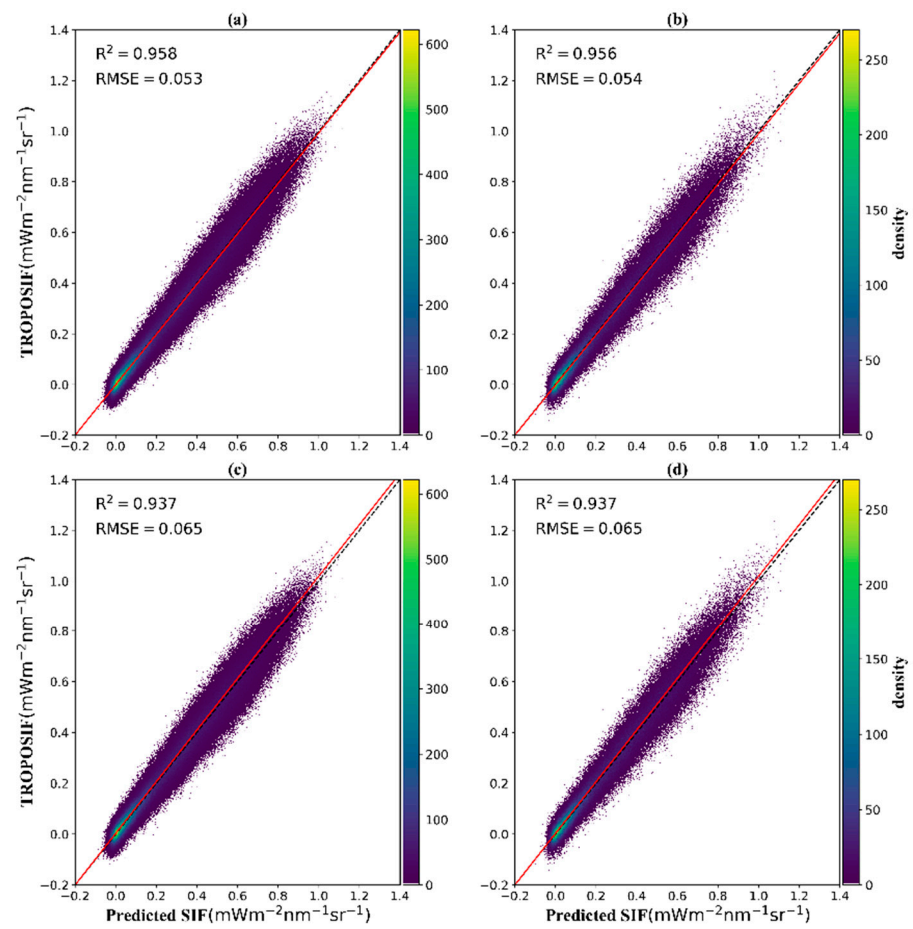**Figure 3.** The probability distribution of residuals (TROPOSIF minus predicted TSIF).

Figure 4. The scatterplots of TROPOSIF and predicted TSIF for training and validation; (**a**,**b**) for our local models and (**c**,**d**) for the universal model.
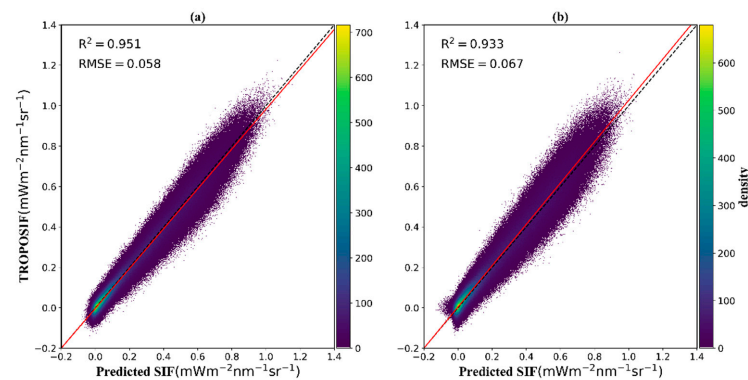
Figure 5. The scatterplots of TROPOSIF and re-aggregated SIF; (**a**) for our local models and (**b**) for the universal model.

To further explore the performance advantage of our local models over that of the universal model, we also calculated the temporal correlations of each pixel between TROPOSIF and TSIF, and TROPOSIF and USIF. As shown in Figure 6a, for TSIF, 85% of the pixels have a temporal correlation with $R^2 > 0.9$ and 92% of pixels with $R^2 > 0.85$. However, for USIF, 79% of pixels $R^2 > 0.9$ and 92% of pixels had $R^2 > 0.85$; 80% of R^2 of TSIF are greater than R^2 of USIF. This finding suggests that our local models can capture better temporal information in TROPOSIF than the universal model for almost all land cover types within the MODIS tile grid H27V05; a reasonable explanation is that the universal model learns the data features only from the value distribution of the samples and learns the temporal features indirectly from the value changes of samples. In Figure 6a,b, only a small portion of TSIF pixels exhibit slightly lower correlations in the lower left of the images where we found many data gaps caused by cloud contamination.
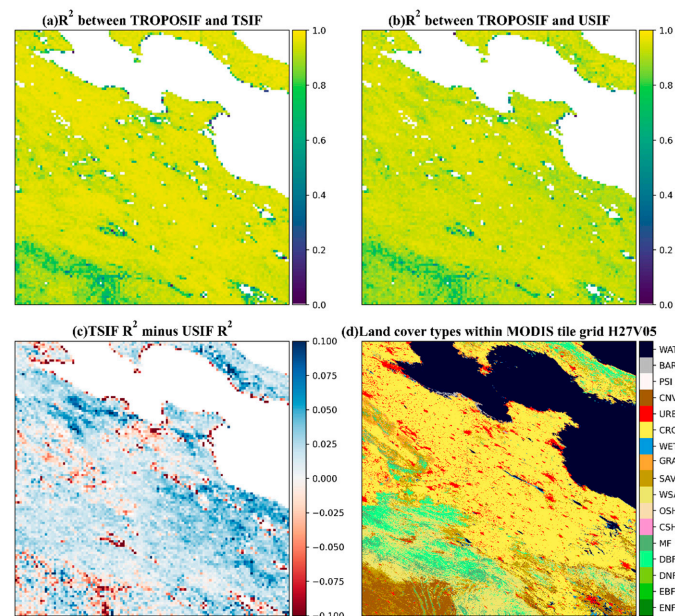

Figure 6. The temporal correlations of (**a**) TROPOSIF and TSIF and of (**b**) TROPOSIF and USIF; (**c**) the difference of TSIF R^2 minus USIF R^2, R^2 refers to the temporal correlation; (**d**) the land cover types within the MODIS tile grid H27V05. The abbreviations are as follows: ENF, Evergreen Needleleaf Forests; EBF, Evergreen Broadleaf Forests; DNF, Deciduous Needleleaf Forests; DBF, Deciduous Broadleaf Forests; MF, Mixed Forests; CSH, Closed Shrublands; OSH, Open Shrublands; WSA, Woody Savannas; SAV, Savannas; GRA, Grasslands; WET, Permanent Wetlands; CRO, Croplands; URB, Urban and Built-up Lands; CNV, Cropland/Natural Vegetation Mosaics; PSI, Permanent Snow and Ice; BAR, Barren; WAT, Water Bodies.

We also calculated the mean and the 5th and 95th percentile of *SIF* of all pixels from TROPOSIF, TSIF, and USIF, respectively. As shown in Figure 7, both our local models and the universal can capture well the temporal variations in TROPOSIF, with the 5th percentile, the 95th percentile, and the mean of predicted *SIF* resembling that of the original TROPOSIF. The strong consistency holds under both normal and stressed conditions. For example, in July 2019, the area within the MODIS tile grid H27V05 suffered a severe drought, and the TSIF below the normal was successfully captured. We observed some discrepancies in temporal variations between TSIF, USIF, and the original TROPOSIF. For example, on 10 June 2018, the 95th percentile of TSIF shows a slight offset from TROPOSIF. The case is likely due to human agricultural activities (e.g., irrigation), but USIF has more such discrepancies. In general, TSIF better captures the temporal variations in TROPOSIF than USIF.
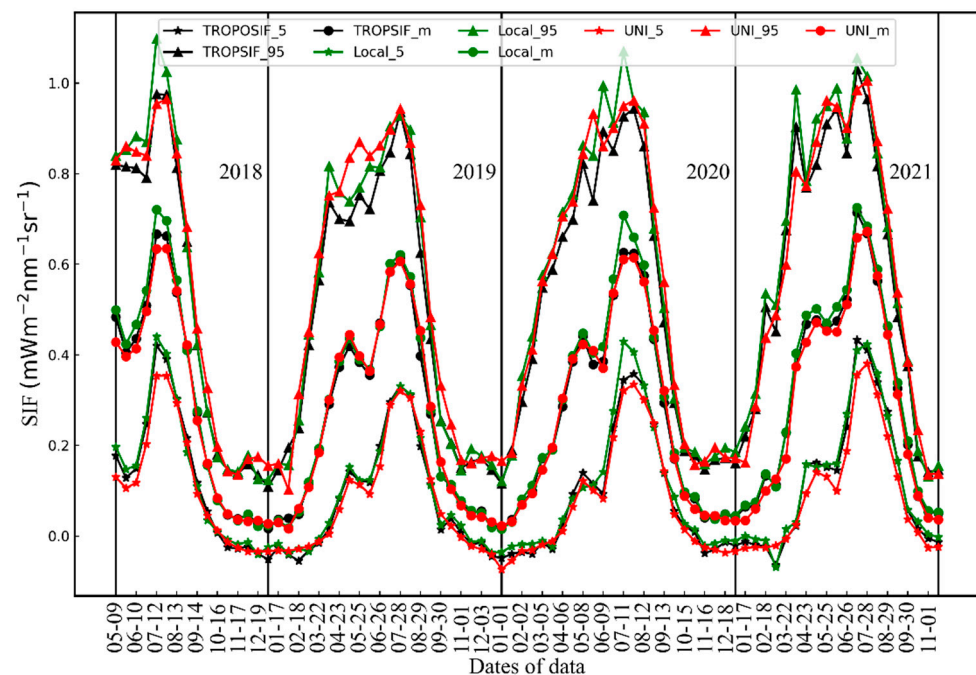

Figure 7. TROPOSIF_5, TROPOSIF_95, and TROPOSIF_m means in the 5th percentile, the 95th percentile, and the mean of TROPOSIF, respectively; TSIF_5, TSIF_95, and TSIF_m are the 5th percentile, the 95th percentile and the mean of TSIF, respectively; UNI_5, UNI_95, and UNI_m are the 5th percentile, the 95th percentile, and the mean of USIF, respectively.

3.1.2. Validation of Our Method's Robustness against Overfitting

The machine learning model relies on sufficient samples to achieve high accuracy and to avoid overfitting. Because we only used a small number of samples from regional data and individual data to train each local model, overfitting must be considered. Although similar methods using regional data have been often applied to surface temperature (LST) downscaling, applying such a method to *SIF* downscaling studies has not been thoroughly discussed and analyzed. We set the complexity of the models by changing the numbers of hidden layers and neurons to test the robustness of local models against overfitting. A total of 23 scenes of MODIS data and TROPOSIF in 2020 were used to generate individual local models with different complexity. We used the absolute differences between the training R^2 and the validation R^2 as the evaluation metrics of overfitting. The smaller the R^2 difference is, the less likely it is that overfitting occurs. As shown in Figure 8, the difference between the training R^2 and the validation R^2 does not change much as the numbers of neurons and hidden layers change, and most of the differences are relatively small, generally below 0.04. This suggests that the changes in hidden layers and neurons do not change the local models' performance significantly, indicating the local models have a strong resistance to

overfitting to some extent. The possible reason is that the training dataset and validation dataset have similar features (e.g., value distribution and temporal characteristics).
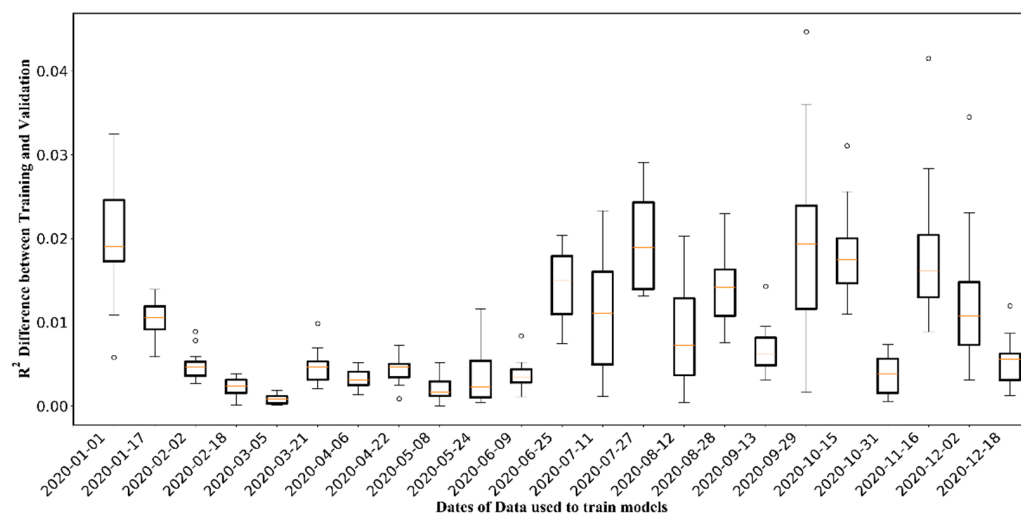

Figure 8. The boxplots of R^2 difference from different NN models with the numbers of layers changing from 1 to 4 and the numbers of neurons of the hidden layers changing from 8 to 64 (the absolute value of the training R^2 minus the validation R^2). Each boxplot contains the R^2 difference specific to one date.

3.1.3. Spatiotemporal Patterns of TSIF

Figure 9 shows that TSIF captures well the *SIF* signal in TROPOSIF observations, but provides more detailed information. TSIF shows the expected spatial and temporal variations. In January (the coldest month of winter, Figure 9a,b), because the area within MODIS tile grid H27V05 is dry and cold, the photosynthetic activity of all plants is limited, so both TSIF and TROPOSIF are very small. From February (the last month of winter, Figure 9c,d) to April (spring, Figure 9e–h), because the temperature gradually increases and vegetation show stronger and stronger photosynthetic activity, both TSIF and TROPOSIF increase gradually. During this period, the hotspot is observed in cropland located in the center of the images in the Sinusoidal coordinate reference system, and the hotspot spreads from the center to the upper left of the images (corresponding from the center to the north in the WGS84 coordinate reference system). Meanwhile, other plants such as DBF, SAV, and CNV show increasingly stronger photosynthetic activity. The right upper part of the images, corresponding to the Korean Peninsula in the WGS84 coordinate reference system, shows relatively small *SIF* due to low temperatures. In May (spring) and June (summer), the DBF located at the bottom left of the images (Figure 9i–l) shows the strongest photosynthetic activity with the highest *SIF* observed. During this period, most crops enter the mature and harvest stages. In July (summer, Figure 9m,n), when crops have been sown and enter the growing stage again, both DBF and croplands display active photosynthesis with the highest SIF. In fact, July is the month when almost all plants show the strongest photosynthesis due to high temperatures and sufficient precipitation. From August, photosynthesis starts to decrease for most plants, they show smaller *SIF* compared to July, while croplands still show a hotspot from the upper left to the bottom right of the images (Figure 9o,p). In September (autumn), crops enter the mature stage again, showing lower *SIF* compared to August. In October (autumn), crops enter their harvest stage and all plants show relatively low *SIF* due to low temperatures. In November (autumn) and December (winter), all plants show low *SIF* due to dry and cold weather, with the highest *SIF* observed in cropland again.
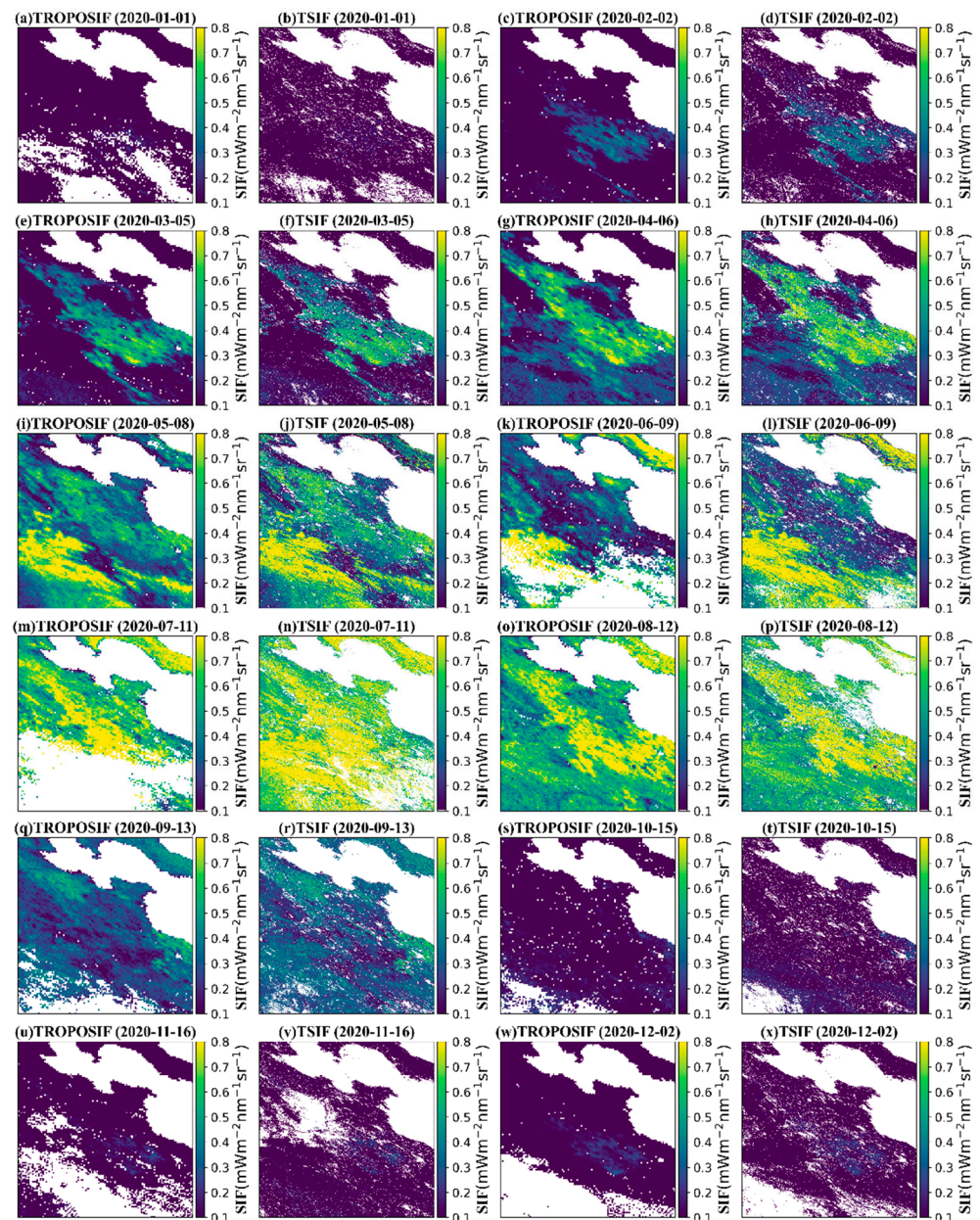
Figure 9. Spatial and temporal patterns of TSIF and TROPOSIF from January to December in 2020. White means no data due to pixel removal of water, barren and built-up, or cloud contamination (**a–x**).

As shown in Figure 10, we select several 3 × 3 grids from TROPOSIF and the corresponding 60 × 60 grids from TSIF and MCD12Q1 land cover classification for further analysis. Figure 10a,d,g show TROPOSIF data are too coarse to capture any details, but TSIF is able to show more details. For example, in Figure 10b, TSIF can distinguish OSH from ENF to some extent, in Figure 10h, TSIF can distinguish SAV from CNV clearly. In general, the downscaled TSIF can provide more details which will benefit many applications.

3.1.4. Comparison of CASIF and Tower GPP

To compare TSIF with CASIF, we first generated the mosaics of three MODIS tiles (H09V05, H09V05, and H09V05) from May 2018 to December 2021 and extracted the subset of the mosaics covering California (columns from 1 to 2800, rows from 1 to 3500). We then aggregated TROPOSIF corresponding to the subset and trained the models with the same configuration mentioned above using the MODIS subset data and TROPOSIF. Finally, we generated TSIF.
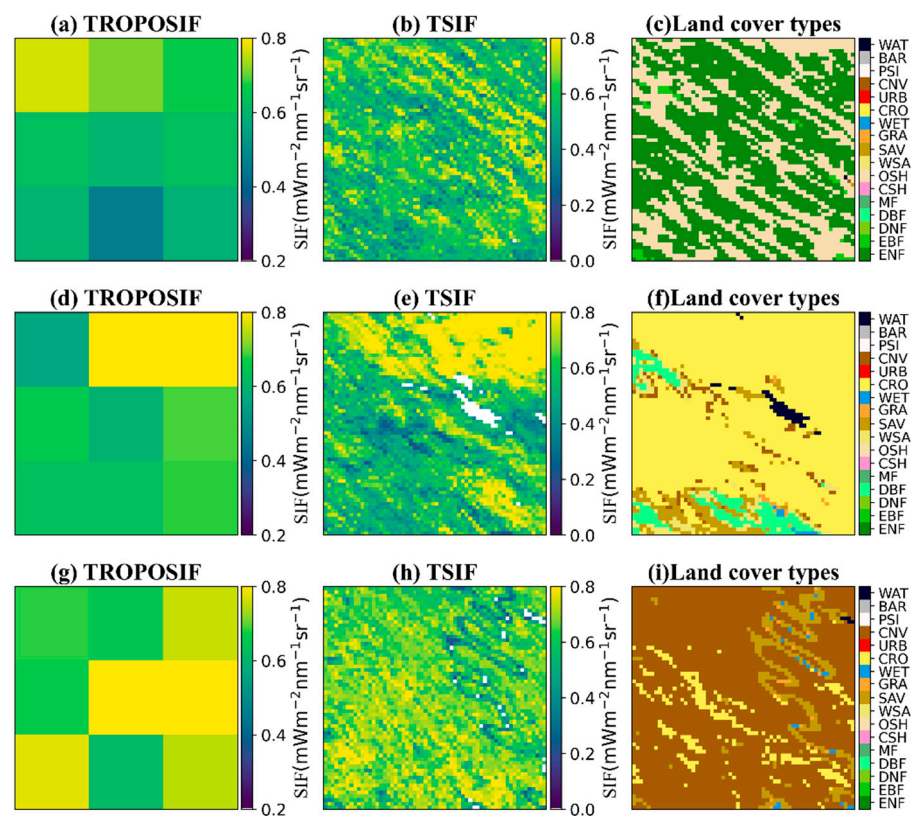
Figure 10. The spatial details of the downscaled TSIF; (**a**,**d**,**g**) are 3 × 3 grids from TROPOSIF; (**b**,**e**,**h**) are 60 × 60 grids of TSIF corresponding to (**a**,**d**,**g**); and (**c**,**f**,**i**) are 60 × 60 grids from MCD12Q1 land cover (2019). TROPOSIF and TSIF data correspond to MODI Grid Tile H27V05 and the date of the data is 28 July 2019.

TSIF can capture similar spatial patterns as CASIF. Figure 11 shows an example for April and June. TSIF is in good spatial agreement with CASIF, but with a smaller magnitude; we used daily *SIF* instead of instantaneous SIF. We also did not calculate the temporal correlation of each pixel between TSIF and CASIF because the daily correction factor used in TROPOSIF SIF_Corr_743 may introduce nonlinearities compared to CASIF. However, at six AmeriFlux eddy covariance sites, TSIF showed a strong temporal correspondence with CASIF and GPP (measured from 12:00 to 14:00 corresponding to the overpass time of TROPOMI) across four different ecosystems (corn, woody savanna, grassland, and wetland) (Figure 12). We found that TSIF can capture similar features of photosynthetic activity of different ecosystems as CASIF does; for example, both TSIF and CASIF can clearly capture the onset of photosynthesis as well as the seasonal cycle of GPP in a cornfield (US-Bi2) (Figure 12a).

In order to further explore the SIF-GPP relationship, we also drew the scatterplots of TSIF and GPP as shown in Figure 13. The tower GPP was aggregated temporally to 16-day to match TSIF's temporal resolution. The results show that TSIF is very strongly correlated with GPP with $R^2 > 0.81$ except for one site (US-TW4, $R^2 = 0.58$). The slopes range from 11.56 to 22.18.
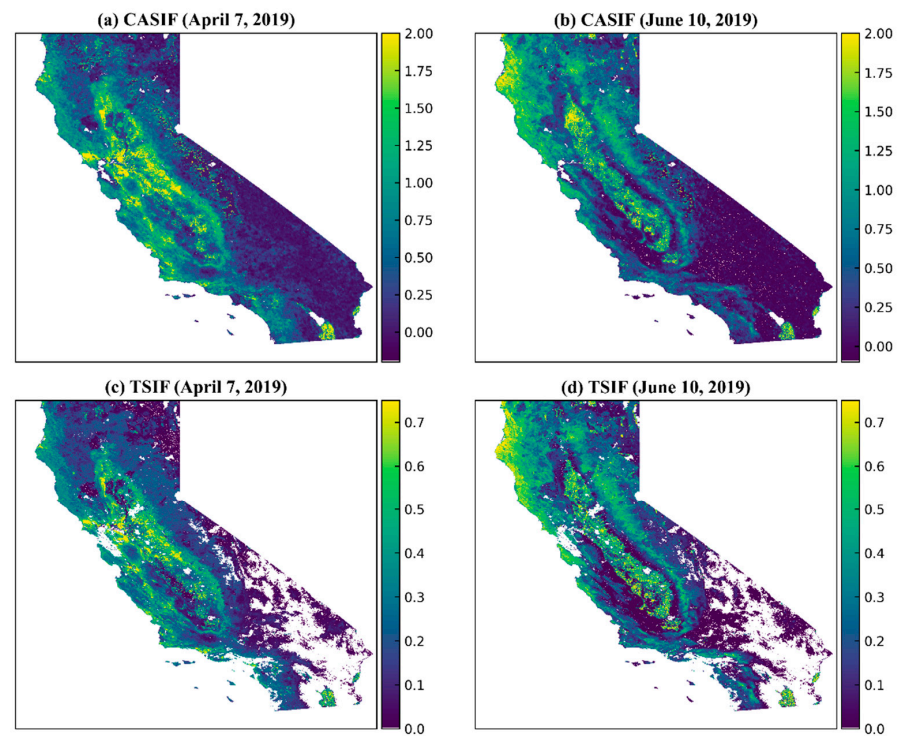
Figure 11. (**a**,**b**) CASIF and (**c**,**d**) TSIF on 7 April 2019 and 10 June 2019. CASIF are temporally aggregated to 16-day. The data gaps result from missing data in MODIS or TROPOSIF.
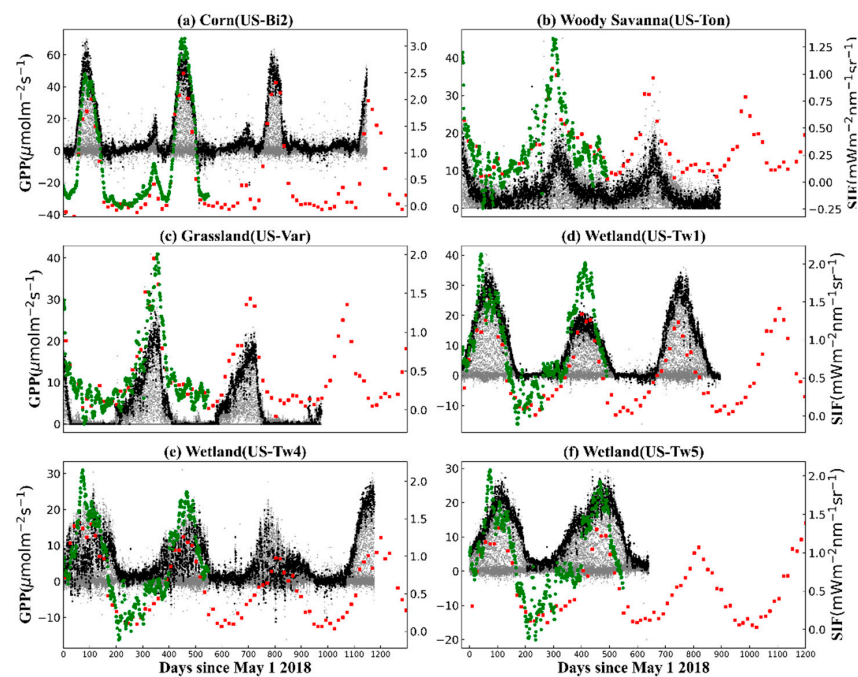

Figure 12. Time series of CASIF, TSIF, and GPP at six eddy covariance sites from AmeriFlux. Black points are the GPP measurements between 12:00 and 14:00 corresponding to the overpass time of TROPOMI; gray points represent all GPP measurements from six eddy covariance sites; green points represent CASIF; red points represent TSIF. The left axis is for GPP, the right axis is for SIF. The *x*-axis shows the number of days since 1 May 2018 (**a**–**f**).
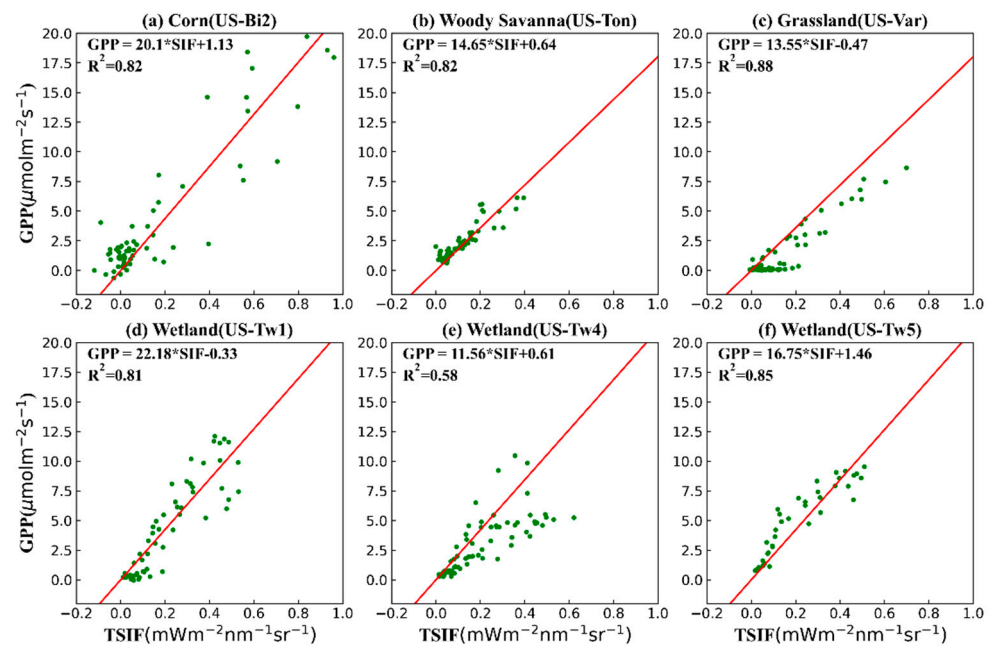
Figure 13. Scatterplots of GPP and TSIF from six eddy covariance sites of AmeriFlux over four different ecosystems (corn, woody savanna, grassland, and wetland) (**a**–**f**). The GPP was temporally aggregated to 16-day to match the temporal resolution of TSIF. Red lines are the regression lines.

In Turner's work [24], one of the most significant features is the apparent double peak in the seasonal cycle of SIF. The time series of TSIF in California (Figure 14), shows the same double peak feature in the seasonal cycle of croplands (CRO), evergreen needleleaf forests (ENF), and the statewide TSIF mean. Moreover, the results also suggest that the SIF-GPP relationship at coarse temporal resolution (16-day) is stronger than that at fine temporal resolution (daily) when compared to Turner's finding [24].
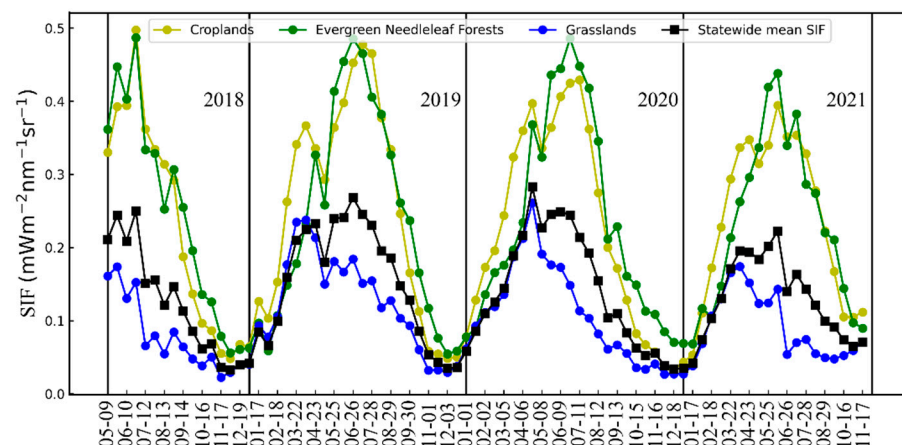

Figure 14. Time series of TSIF in California. The land cover types were from the MCD12Q1.006 land cover dataset (IGBP) classification. Croplands, evergreen needleleaf forests, and grasslands mean the TSIF is calculated using the TSIF pixels of croplands, evergreen needleleaf forests, and grasslands, respectively. Statewide mean *SIF* means the TSIF is calculated using all the TSIF pixels in California.

3.2. SIF Response to Henan Drought in 2019

3.2.1. Spatial and Temporal Patterns of Drought

Henan suffered a severe drought in July 2019 when there was a precipitation deficit of 10–90% across Henan compared to the multi-year average while temperatures were 0.1–3.2 °C above the multi-year average in most areas of Henan. Autumn grain production

decreased by 2.8% compared to the previous year 2018. The drought was alleviated by extreme precipitation in early-mid August of the same year (http://henan.weather.com.cn/ (accessed on 2 November 2021)). The drought and extreme precipitation provide an ideal opportunity to explore the ability of our TSIF for drought monitoring.

As shown in Figure 15a,b, SPEI shows a severe meteorological drought in July 2019, when the northwestern, western, and southern parts of Henan suffered severe or extreme drought, while the other parts suffered moderate drought. The drought continued in August in the southern part of Henan. As shown in Figure 16a,b, we calculated the monthly precipitation anomalies using Chirps2 monthly precipitation data from 1981 to 2021. The precipitation deficit across Henan in July was also observed with negative precipitation anomalies, and spatial patterns of the drought characterized by the precipitation anomalies were similar to those characterized by SPEI. In August, the western, northwestern, and northern parts of Henan received more precipitation than the multi-year average, with positive precipitation anomalies indicating the drought in these areas was alleviated to some extent. The central and southern parts of Henan showed negative precipitation anomalies, indicating that the precipitation deficit continued in August in these areas. As shown in Figure 15c,d, SPEI shows that no drought event occurred in July 2018; the western part of Henan suffered severe or extreme drought and the other parts show no drought in August 2018; precipitation anomalies show a precipitation deficit in the central, eastern, and southern parts of Henan in July 2018, and the western part and southern part of Henan in August 2018 (Figure 16c,d).
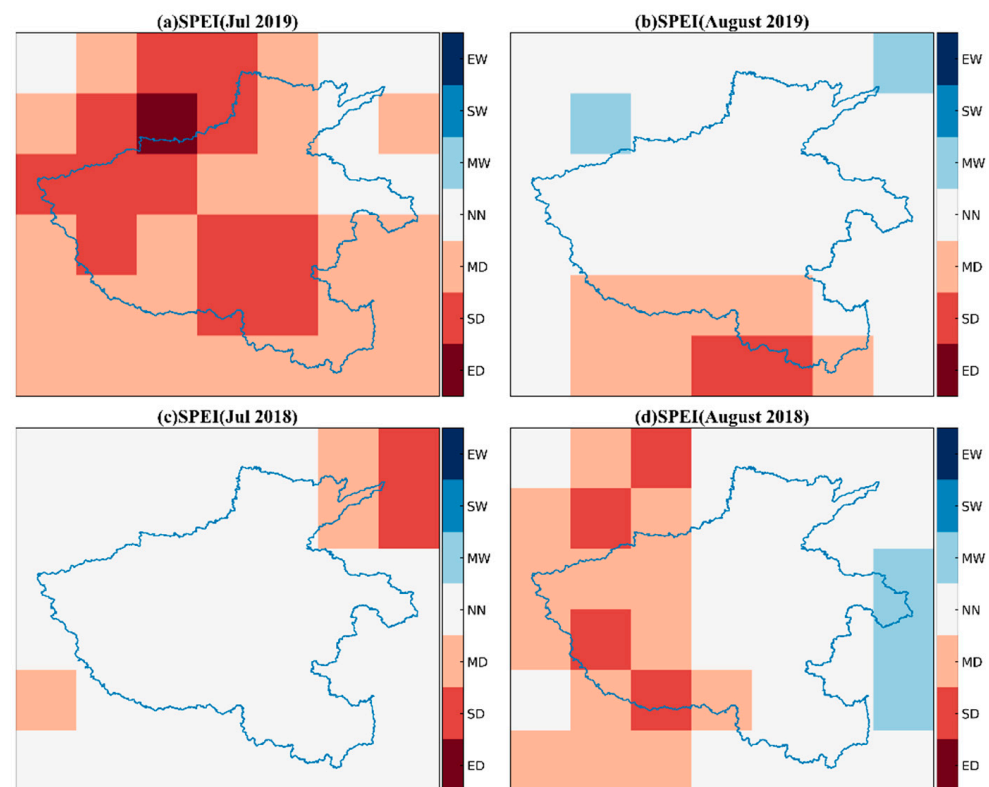

Figure 15. Spatial and temporal patterns of drought characterized by SPEI for July (**a**,**c**) and August (**b**,**d**) of 2018 and 2019. The abbreviations are as follows: EW, extremely wet; SW, severely wet; MW, moderately wet; NN, near normal; MD, moderately dry; SD, severely dry; ED, extremely dry.
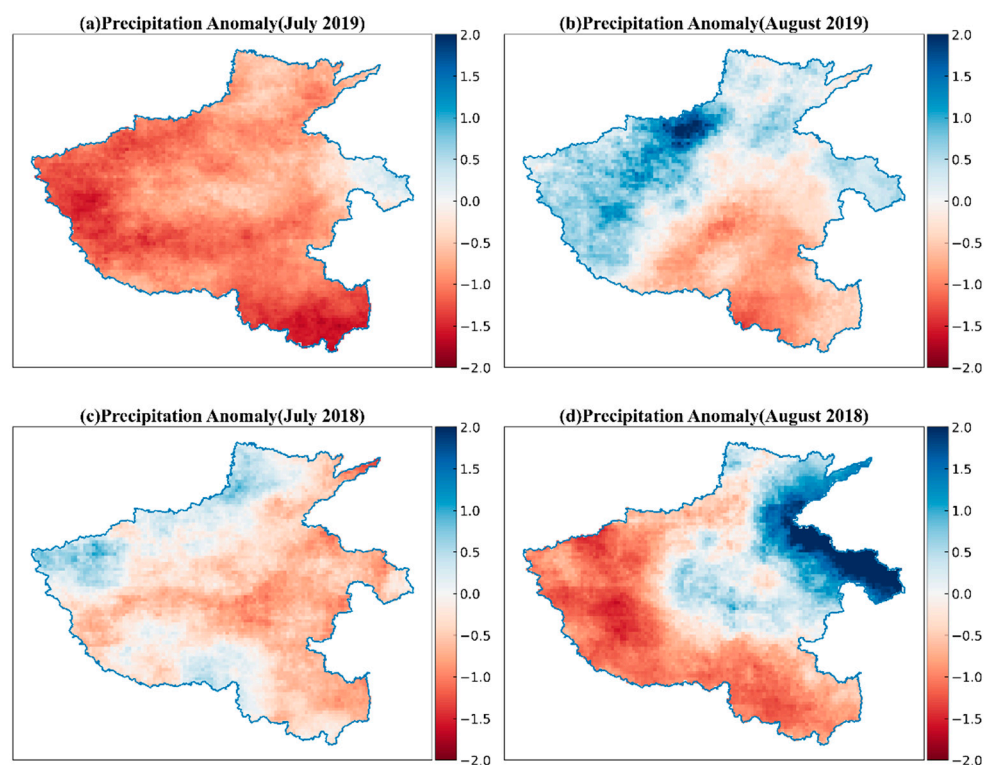
Figure 16. Spatial and temporal patterns of drought characterized by precipitation anomalies for July (**a**,**c**) and August (**b**,**d**) of 2018 and 2019.

3.2.2. Response of *SIF* to Drought

Because TROPOMI has a relatively short mission length, starting from October 2017, and TROPOSIF L2B is only available from May 2018 to December 2021 (at the time of the study), we did not calculate the anomalies of TSIF which generally require at least five years of data. We selected 2018 as the reference year to compute the relative difference (defined in Equation (1)) to characterize the drought event. Note that the wetter areas in the reference year will reduce the relative differences and the drier areas will increase the relative differences.

As shown in Figure 17, the spatial and temporal patterns and magnitude of TSIF-Diff are consistent with TROPOSIF-Diff but with more detailed information. In general, TSIF-Diff shows negative values in most of Henan Province in July 2019, indicating that the drought limited the photosynthetic activity and resulted in lower *SIF* compared with that in 2018. The drought observed by the relative differences (including TROPOSIF-Diff, TSIF-Diff, USIF-Diff, EVI-Diff, and NDVI-Diff) is consistent in spatial pattern with the drought observed by SPEI and PPT anomalies in July 2019. The results show that TROPOSIF-Diff, TSIF-Diff, USIF-Diff, EVI-Diff, and NDVI-Diff can capture the overall drought. Specifically, TSIF has an average decline of 14.8%, TROPOSIF by 13.2%, USIF by 4.7%, EVI by 10.4%, and NDVI by 9.8% on July 12 compared to 12 July 2018. TSIF and TROPOSIF have larger responses to drought, followed by EVI, NDVI, and USIF. USIF-Diff, EVI-Diff, and NDVI-Diff show a wetter southern Henan (Figure 17g,j,m), while the drought was captured by TROPOSIF-Diff and TSIF-Diff, which is likely due to the fact the universal model cannot capture the temporal variations well in TROPOSIF and EVI and NDVI has a long lag to drought. Some pixels corresponding to DBF located in the western part of Henan show positive differences, indicating that they did not suffer drought stress compared to 2018. Possible reasons for this are 1) the wetter June received sufficient precipitation and DBF have deep roots that can absorb water from deeper soil; 2) higher temperature enhances photosynthetic activity. On July 28, 2019, TSIF shows an average decline of 6.6%, TROPOSIF of 7.7%, USIF of 1.1%, EVI of 2.0%, and NDVI of 3.2%. TROPOSIF and TSIF

also have the largest responses to drought, followed by NDVI, EVI, and USIF. As shown in Figure 17b,e,h,k,n, the drought area of DBF in western Henan increased as the drought continued, which can also be characterized by TROPOSIF-DIFF and TSIF-Diff; however, USIF-Diff shows a wetter western Henan (Figure 17h). The drought in southern Henan also intensified according to the relative differences between *SIF* and EVI.
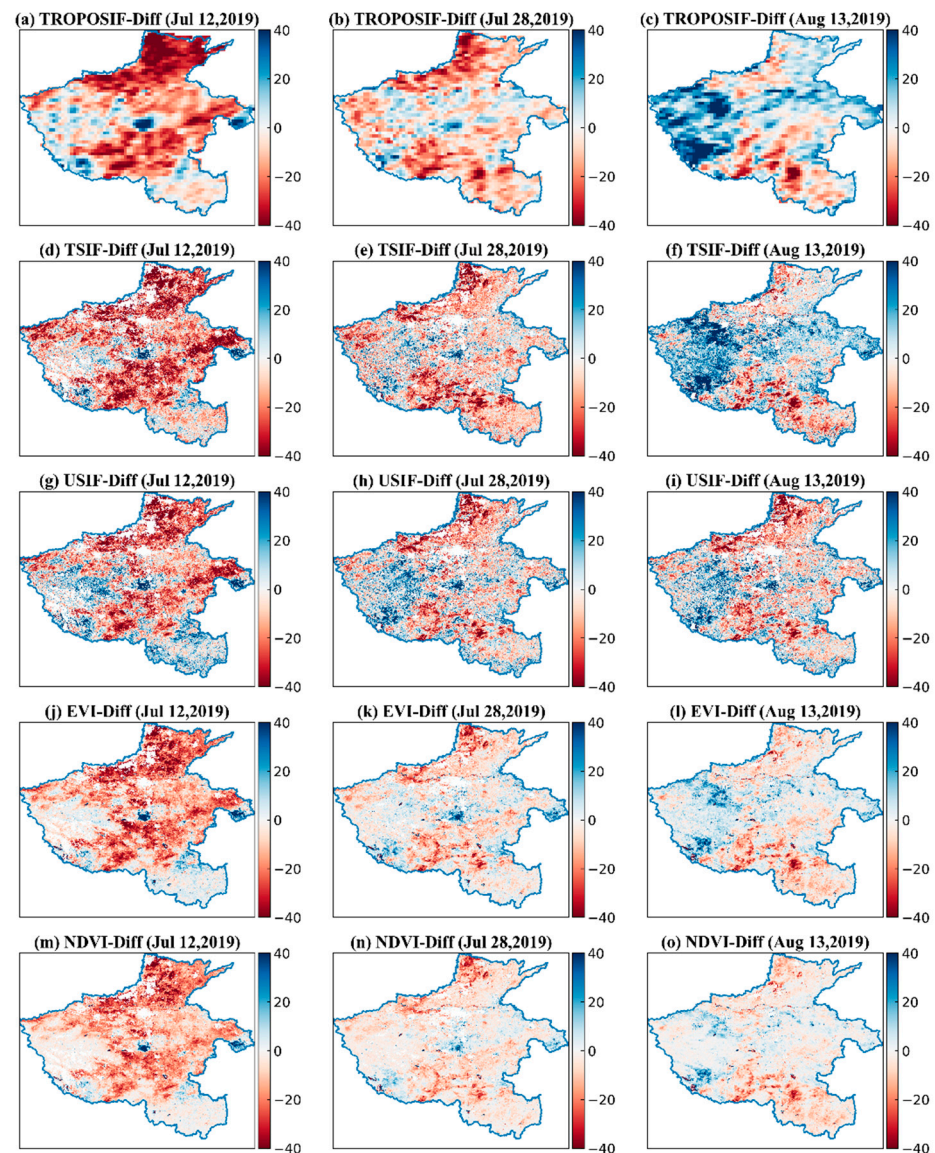

Figure 17. Spatial and temporal patterns of drought characterized by TROPOSIF-Diff (**a–c**), TSIF-Diff (**d–f**), USIF-Diff (**g–i**),EVI-Diff (**j–l**), and NDVI-Diff (**m–o**) for July and August of 2019.

On 13 August 2019, TSIF shows an average increase of 7.3%, TROPOSIF of 6.5%, USIF of 6.6% EVI of 0.35% and NDVI of 0.2% (Figure 17c,f,i,l,o). TROPOSIF-Diff, TSIF-Diff, USIF-Diff, EVI-Diff, and NDVI-Diff indicated a wetter August in Henan, but EVI and NDVI have the smallest increase, followed by TROPOSIF, USIF, and TSIF, indicating that *SIF* is more sensitive to precipitation than EVI.

These results suggest that TSIF-Diff has similar spatial and temporal patterns with TROPOSIF-Diff, and TSIF-Diff can capture well the spatial and temporal variations of drought in Henan compared to USIF-Diff and EVI-Diff. In general, TSIF is more sensitive to drought and precipitation than USIF and EVI.

4. Discussion

We presented an operational downscaling method that can generate a 500 m 16-day *SIF* product using TROPOSIF and MODIS data over a local spatiotemporal window. Similar methods have been widely used for LST downscaling [27–29] and the same idea has also been used in *SIF* downscaling in previously published studies [14,15]. For example, Yu et al. [14] used a machine learning method stratified by biomes and times for training and predictions to generate a 0.05° 16-day OCO-2-derived reconstructed *SIF* product [14]. Wen et al. used a machine learning method imposed with regionalization constraints to account for relationships between explanatory variables and *SIF* in space and time to generate a long time series of a *SIF* product at 0.05° and monthly resolution [8]. However, they only provide coarse resolution reconstructed *SIF* at 0.05°. Due to the sparse sampling strategy and a long revisit period of OCO-2 and TanSat, training a local model stratified by space and time is impossible for small regions. For other very coarse satellite-observed SIF, the very coarse resolution hinders further resolution enhancement. While *SIF* applications for drought monitoring have been explored, to the best of our knowledge, no high-resolution *SIF* has been used. We selected six bands of reflectance data from MCD43A4 and fPAR and LAI from MCD15A2 as our explanatory variables because many studies have shown the BRDF reflectance is a valid explanatory variable and widely used to generate *SIF* products. We did not select band Band6, because we found that it makes a small contribution to the improvement of the model performance and has too many data gaps in our study area. We selected fPAR because it is one of the components of *SIF* according to [22]. LAI is related to the *SIF* escape factor [30]. We did not use ET and LST due to too many data gaps, which would reduce the usability of the downscaled SIF.

During the aggregation of TROPOSIF, we calculated the average of all pixels falling within the aggregated grid cells, which is an approach used in many studies [11,12,14]. This approach did not allow for *SIF* footprint geometry and vegetation fraction [15,24]. In Turner's work, *SIF* was aggregated, allowing for vegetation fraction as a weighting factor which assumes that *SIF* from TROPOMI originates from more vegetated regions. In the future, we will test the differences between different aggregation methods. In addition, as the residuals between TROPOSIF and TSIF show a strong seasonal cycle, it suggests there are still some variations in TROPOSIF that cannot be learned fully due to the 16-day time step, but in general, TSIF reproduces TROPOSIF very well.

Our results also show that TSIF has a better temporal consistency with TROPOSIF compared to USIF. The universal model only learns features of samples by the value distribution and learns the temporal features indirectly from the value changes of the samples. So, some studies used the local models to generate downscaled *SIF* instead of the universal model [14,15,31].

During the training process, we found that our method is robust against overfitting. The most reasonable reason is that training data and validation data have common distribution and temporal features which reduce the uncertainties caused by variations in data distribution and seasonality. The data used for fine resolution *SIF* generation also have similar data distribution and temporal features because the coarse-resolution aggregated MODIS data are simply the average of the fine resolution pixels.

The use of *SIF* for drought monitoring has been widely explored. Sun et al. applied GOME-2 *SIF* to monitor the Texas droughts in 2011 and the central Great Plains drought in 2012 and found the spatial patterns of *SIF* anomalies very much resembled drought intensity maps from the U.S. Drought Monitor for both events and that *SIF* is sensitive to both structural and physiological/biochemical variations of vegetation caused by drought [3]. Shekhar et al. used OCO-2 *SIF* to monitor the 2018 European drought and found that *SIF* is more sensitive to drought than MODIS's fPAR and NDVI [4]. In fact, *SIF* has been also used to monitor the Russian drought in 2010 [5], and the northern Great Plain drought in 2017 [6]. The results show that *SIF* is a promising indicator of drought. However, there are very few studies using the relatively high-resolution *SIF* (e.g., 500 m) for drought monitoring due to the lack of high-resolution downscaled SIF, and because TROPOSIF

has a very short mission length, we cannot obtain a long time series of TSIF dataset which hinders TSIF applications in drought monitoring. Thus, we used a relative difference as evaluation metrics for drought monitoring, which only uses two years of data, overcoming this problem to some extent. Similar methods have also been used in vegetation growth monitoring studies [32] and drought monitoring [14]. The results show that TSIF-Diff can capture almost the same spatial and temporal patterns as TROPOSIF-Diff and can capture the spatiotemporal patterns of drought. In addition, TSIF-Diff is more sensitive to drought and precipitation compared to USIF-Diff and EVI-Diff. In the future, the TSIF anomalies can also be calculated when TROPOMI has 5 years of *SIF* observations.

TSIF has many data gaps caused by MODIS data gaps. In the future, we will test different methods for gap-filling without introducing large uncertainties. Moreover, because we aim to develop an operational downscaling method, we did not perform strict quality control on data to avoid too many data gaps, which will introduce some uncertainties. TSIF has a temporal resolution of 16-day, finer temporal resolution downscaled *SIF* (e.g., 8-day and 4-day) are also needed. A suitable downscaling method will be tested in the future. Finally, different land covers may represent different relationships between explanatory variables and *SIF* in different regions and times, these factors will also be allowed for in the future.

Because our method only needs regional data instead of global data for training the downscaling models, the downscaling models can be trained quickly and easily. We can generate downscaled *SIF* in a given area without having to collect and process significant amounts of data. Our method is very practical.

5. Conclusions

We presented an operational downscaling method of Solar-Induced Chlorophyll Fluorescence for regional drought monitoring. The method uses only regional MODIS data and TROPOSIF data for training and prediction of the local model, making it easier to update and reproduce machine learning models. The relatively high observation frequency and spatially continuous coverage of TROPOMI make it possible to obtain high-resolution downscaled *SIF* and train machine learning models over small regions due to sufficient sample sizes. The spatiotemporal patterns of the downscaled TSIF show a very strong consistency with satellite derived TROPOSIF but at a finer resolution. TSIF can also reproduce TROPOSIF with the same magnitude and variation. A comparison between CASIF and tower GPP showed that TSIF is consistent in spatial and temporal patterns with CASIF and displayed a strong temporal consistency with tower GPP over six eddy covariance sites. Moreover, TSIF can also capture the double peak in the seasonality of California's photosynthesis found in Turner's work [24]. TSIF shows a strong correlation with GPP with $R^2 > 0.81$, except for one site ($R^2 = 0.58$). Finally, we used the relative difference TSIF-Diff for drought monitoring which captured well the spatial and temporal patterns of drought and was more sensitive to drought and precipitation compared to the universal SIF-Diff and EVI-Diff. In general, our *SIF* is a promising indicator for regional drought monitoring.

Author Contributions: Conceptualization, Z.H. and L.M.; methodology, Z.H., Y.H. and L.M.; software, Z.H., W.L. and C.C.; validation, Y.H., C.C., W.Z. and L.L.; formal analysis, W.Z. and C.T.; investigation, L.M.; resources, C.C.; data curation, Z.H.; writing—original draft preparation, Z.H.; writing—review and editing, X.Y.; visualization, C.C. and C.T.; supervision, L.M.; project administration, L.M.; funding acquisition, L.M. All authors have read and agreed to the published version of the manuscript.

Institutional Review Board Statement: Not applicable.

Informed Consent Statement: Not applicable.

Conflicts of Interest: The authors declare no conflict of interest.

References

1. Grace, J.; Nichol, C.; Disney, M.; Lewis, P.; Quaife, T.; Bowyer, P. Can We Measure Terrestrial Photosynthesis from Space Directly, Using Spectral Reflectance and Fluorescence? *Glob. Chang. Biol.* **2007**, *13*, 1484–1497. [CrossRef]
2. Sellers, P.J. Canopy Reflectance, Photosynthesis and Transpiration. *Int. J. Remote Sens.* **1985**, *6*, 1335–1372. [CrossRef]
3. Flexas, J.; Escalona, J.M.; Evain, S.; Gulías, J.; Moya, I.; Osmond, C.B.; Medrano, H. Steady-State Chlorophyll Fluorescence (Fs) Measurements as a Tool to Follow Variations of Net CO_2 Assimilation and Stomatal Conductance during Water-Stress in C3 Plants. *Physiol. Plant.* **2002**, *114*, 231–240. [CrossRef]
4. Baker, N.R. Chlorophyll Fluorescence: A Probe of Photosynthesis In Vivo. *Annu. Rev. Plant Biol.* **2008**, *59*, 89–113. [CrossRef]
5. Daumard, F.; Champagne, S.; Fournier, A.; Goulas, Y.; Ounis, A.; Hanocq, J.-F.; Moya, I. A Field Platform for Continuous Measurement of Canopy Fluorescence. *IEEE Trans. Geosci. Remote Sens.* **2010**, *48*, 3358–3368. [CrossRef]
6. Frankenberg, C.; Fisher, J.B.; Worden, J.; Badgley, G.; Saatchi, S.S.; Lee, J.-E.; Toon, G.C.; Butz, A.; Jung, M.; Kuze, A.; et al. New Global Observations of the Terrestrial Carbon Cycle from GOSAT: Patterns of Plant Fluorescence with Gross Primary Productivity. *Geophys. Res. Lett.* **2011**, *38*, 17. [CrossRef]
7. Joiner, J.; Yoshida, Y.; Vasilkov, A.P.; Yoshida, Y.; Corp, L.A.; Middleton, E.M. First Observations of Global and Seasonal Terrestrial Chlorophyll Fluorescence from Space. *Biogeosciences* **2011**, *8*, 637–651. [CrossRef]
8. Frankenberg, C.; O'Dell, C.; Berry, J.; Guanter, L.; Joiner, J.; Köhler, P.; Pollock, R.; Taylor, T.E. Prospects for Chlorophyll Fluorescence Remote Sensing from the Orbiting Carbon Observatory-2. *Remote Sens. Environ.* **2014**, *147*, 1–12. [CrossRef]
9. Du, S.; Liu, L.; Liu, X.; Zhang, X.; Zhang, X.; Bi, Y.; Zhang, L. Retrieval of Global Terrestrial Solar-Induced Chlorophyll Fluorescence from TanSat Satellite. *Sci. Bull.* **2018**, *63*, 1502–1512. [CrossRef]
10. Köhler, P.; Frankenberg, C.; Magney, T.S.; Guanter, L.; Joiner, J.; Landgraf, J. Global Retrievals of Solar-Induced Chlorophyll Fluorescence With TROPOMI: First Results and Intersensor Comparison to OCO-2. *Geophys. Res. Lett.* **2018**, *45*, 10456–10463. [CrossRef]
11. Duveiller, G.; Filipponi, F.; Walther, S.; Köhler, P.; Frankenberg, C.; Guanter, L.; Cescatti, A. A Spatially Downscaled Sun-Induced Fluorescence Global Product for Enhanced Monitoring of Vegetation Productivity. *Earth Syst. Sci. Data* **2020**, *12*, 1101–1116. [CrossRef]
12. Li, X.; Xiao, J. A Global, 0.05-Degree Product of Solar-Induced Chlorophyll Fluorescence Derived from OCO-2, MODIS, and Reanalysis Data. *Remote Sens.* **2019**, *11*, 517. [CrossRef]
13. Zhang, Y.; Joiner, J.; Alemohammad, S.H.; Zhou, S.; Gentine, P. A Global Spatially Contiguous Solar-Induced Fluorescence (CSIF) Dataset Using Neural Networks. *Biogeosciences* **2018**, *15*, 5779–5800. [CrossRef]
14. Yu, L.; Wen, J.; Chang, C.Y.; Frankenberg, C.; Sun, Y. High-Resolution Global Contiguous *SIF* of OCO-2. *Geophys. Res. Lett.* **2019**, *46*, 1449–1458. [CrossRef]
15. Wen, J.; Köhler, P.; Duveiller, G.; Parazoo, N.C.; Magney, T.S.; Hooker, G.; Yu, L.; Chang, C.Y.; Sun, Y. A Framework for Harmonizing Multiple Satellite Instruments to Generate a Long-Term Global High Spatial-Resolution Solar-Induced Chlorophyll Fluorescence (SIF). *Remote Sens. Environ.* **2020**, *239*, 111644. [CrossRef]
16. Wang, S.; Luo, X.; Peng, Y. Spatial Downscaling of MODIS Land Surface Temperature Based on Geographically Weighted Autoregressive Model. *IEEE J. Sel. Top. Appl. Earth Obs. Remote Sens.* **2020**, *13*, 2532–2546. [CrossRef]
17. Hutengs, C.; Vohland, M. Downscaling Land Surface Temperatures at Regional Scales with Random Forest Regression. *Remote Sens. Environ.* **2016**, *178*, 127–141. [CrossRef]
18. Sun, Y.; Fu, R.; Dickinson, R.; Joiner, J.; Frankenberg, C.; Gu, L.; Xia, Y.; Fernando, N. Drought Onset Mechanisms Revealed by Satellite Solar-Induced Chlorophyll Fluorescence: Insights from Two Contrasting Extreme Events. *J. Geophys. Res. Biogeosci.* **2015**, *120*, 2427–2440. [CrossRef]
19. Jiao, W.; Chang, Q.; Wang, L. The Sensitivity of Satellite Solar-Induced Chlorophyll Fluorescence to Meteorological Drought. *Earths Future* **2019**, *7*, 558–573. [CrossRef]
20. Liu, L.; Yang, X.; Zhou, H.; Liu, S.; Zhou, L.; Li, X.; Yang, J.; Han, X.; Wu, J. Evaluating the Utility of Solar-Induced Chlorophyll Fluorescence for Drought Monitoring by Comparison with NDVI Derived from Wheat Canopy. *Sci. Total Environ.* **2018**, *625*, 1208–1217. [CrossRef]
21. Helm, L.T.; Shi, H.; Lerdau, M.T.; Yang, X. Solar-Induced Chlorophyll Fluorescence and Short-Term Photosynthetic Response to Drought. *Ecol. Appl.* **2020**, *30*, e02101. [CrossRef] [PubMed]
22. Yoshida, Y.; Joiner, J.; Tucker, C.; Berry, J.; Lee, J.-E.; Walker, G.; Reichle, R.; Koster, R.; Lyapustin, A.; Wang, Y. The 2010 Russian Drought Impact on Satellite Measurements of Solar-Induced Chlorophyll Fluorescence: Insights from Modeling and Comparisons with Parameters Derived from Satellite Reflectances. *Remote Sens. Environ.* **2015**, *166*, 163–177. [CrossRef]

23. Guanter, L.; Bacour, C.; Schneider, A.; Aben, I.; van Kempen, T.A.; Maignan, F.; Retscher, C.; Köhler, P.; Frankenberg, C.; Joiner, J.; et al. The TROPOSIF Global Sun-Induced Fluorescence Dataset from the Sentinel-5P TROPOMI Mission. *Earth Syst. Sci. Data* **2021**, *13*, 5423–5440. [CrossRef]

24. Turner, A.J.; Köhler, P.; Magney, T.S.; Frankenberg, C.; Fung, I.; Cohen, R.C. A Double Peak in the Seasonality of California's Photosynthesis as Observed from Space. *Biogeosciences* **2020**, *17*, 405–422. [CrossRef]

25. Frankenberg, C. Downscaled 500-m TROPOMI *SIF* over California. 2019. Available online: https://data.caltech.edu/records/1327 (accessed on 20 December 2021).

26. Alemohammad, S.H.; Kolassa, J.; Prigent, C.; Aires, F.; Gentine, P. Global Downscaling of Remotely Sensed Soil Moisture Using Neural Networks. *Hydrol. Earth Syst. Sci.* **2018**, *22*, 5341–5356. [CrossRef]

27. Li, W.; Ni, L.; Li, Z.-L.; Duan, S.-B.; Wu, H. Evaluation of Machine Learning Algorithms in Spatial Downscaling of MODIS Land Surface Temperature. *IEEE J. Sel. Top. Appl. Earth Obs. Remote Sens.* **2019**, *12*, 2299–2307. [CrossRef]

28. Ebrahimy, H.; Azadbakht, M. Downscaling MODIS Land Surface Temperature over a Heterogeneous Area: An Investigation of Machine Learning Techniques, Feature Selection, and Impacts of Mixed Pixels. *Comput. Geosci.* **2019**, *124*, 93–102. [CrossRef]

29. Srivastava, P.K.; Han, D.; Ramirez, M.R.; Islam, T. Machine Learning Techniques for Downscaling SMOS Satellite Soil Moisture Using MODIS Land Surface Temperature for Hydrological Application. *Water Resour. Manag.* **2013**, *27*, 3127–3144. [CrossRef]

30. Zhang, Z.; Zhang, Y.; Chen, J.M.; Ju, W.; Migliavacca, M.; El-Madany, T.S. Sensitivity of Estimated Total Canopy *SIF* Emission to Remotely Sensed LAI and BRDF Products. *J. Remote Sens.* **2021**, *2021*, 9795837. [CrossRef]

31. Duveiller, G.; Cescatti, A. Spatially Downscaling Sun-Induced Chlorophyll Fluorescence Leads to an Improved Temporal Correlation with Gross Primary Productivity. *Remote Sens. Environ.* **2016**, *182*, 72–89. [CrossRef]

32. Wu, B.; Meng, J.; Li, Q.; Yan, N.; Du, X.; Zhang, M. Remote Sensing-Based Global Crop Monitoring: Experiences with China's CropWatch System. *Int. J. Digit. Earth* **2014**, *7*, 113–137. [CrossRef]